

# Unraveling the Hierarchic Formation of Open-porous Bimolecular Networks

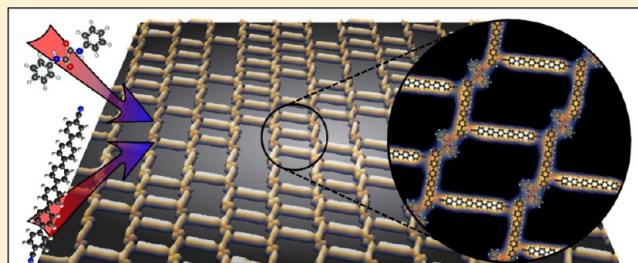
Wolfgang Krenner,<sup>\*,†</sup> Florian Klappenberger,<sup>†</sup> Nenad Kepčija,<sup>†</sup> Emmanuel Arras,<sup>†</sup> Younes Makoudi,<sup>†,§</sup> Dirk Kühne,<sup>†</sup> Svetlana Klyatskaya,<sup>‡</sup> Mario Ruben,<sup>‡,||</sup> and Johannes V. Barth<sup>†</sup>

<sup>†</sup>Department of Physics E20, University of Technology, Munich, James-Franck Straße, 85748 Garching, Germany, and

<sup>‡</sup>Institute of Nanotechnology, Karlsruhe Institute of Technology, 76021 Karlsruhe, Germany

**ABSTRACT:** The surface-confined formation of bicomponent organic molecular networks providing open pores following hierarchic assembly principles is investigated by low-temperature scanning tunneling microscopy and ab initio theoretical methods. The nanomeshes are realized by codeposition of *N,N'*-diphenyl oxalic amide and sexiphenyl dicarbonitrile molecules, with the substrate held at room temperature and subsequent cooling to cryogenic temperatures. We find that the formation of mixed molecular networks is generally preferred over phase segregation.

Depending on the exact stoichiometry of the constituents, different types of open networks self-assemble on the employed Ag(111) surface. All network types reflect hierarchic architectures, where essential molecular interactions are identical and the noncovalent bonding of sexiphenyl to oxalic amide molecules prevails. The different association motifs are assessed by theoretical modeling to unravel the mechanisms mediating the hierarchic organization, whereby a cooperative binding energy enhancement represents a significant factor.



## INTRODUCTION

For the construction of functional nanostructures, molecules as the smallest functional building blocks have been under extensive research in recent years.<sup>1–7</sup> Moreover, investigations toward the realization of functional structures like molecular switches, motors, and rotators have demonstrated the great potential of this surface-confined (supra)molecular chemistry approach.<sup>8–13</sup> Further studies foresee applications in nanomagnetism<sup>14–17</sup> or gas sensing.<sup>18–20</sup> Molecular self-assembly on various surfaces has been studied, leading to nanogratings<sup>21</sup> or open-porous nanomeshes,<sup>22–24</sup> which can be further functionalized or used as templates for the positioning of guest species,<sup>25–28</sup> and to steer their atomic or molecular motion.<sup>29–31</sup>

For the exploration of complex molecular architectures, protocols integrating hierarchic principles due to different binding mechanisms and strengths are of great interest, following intriguing examples found in biological systems.<sup>32–38</sup>

Hierarchic self-assembly requires specific functional groups of the presynthesized building blocks engaged in multiple bond motifs at different organizational levels, thus putting further emphasis on the control over the binding energetics of the systems and the bond-types involved in network formation.<sup>39–47</sup> Moreover, a variety of geometric arrangements can be achieved when multicomponent mixtures self-assemble on the surface.<sup>48–54</sup> Therefore, developing hierarchic organization principles to steer the assembly of nanostructures is an important step toward achieving ultimate control over

formation protocols necessary for functional molecular nano-architectures.

In this work we demonstrate the hierarchic assembly of a multitude of open-porous molecular architectures through the codeposition of chemically functionalized organic molecules, namely *N,N'*-diphenyl oxalic amide (DOA) and sexiphenyl dicarbonitrile (6DC) (see Figure 1 for structure models), on the Ag(111) surface. The investigation was carried out via low-temperature (LT) scanning tunneling microscopy (STM) below 14 K under ultrahigh vacuum (UHV) conditions. We found that the resulting supramolecular structures depend on the stoichiometric ratio and total coverage of the molecular constituents. For all network manifestations the formation of bimolecular chains represents the prevailing hierarchic level and inhibits phase segregation. In superstructures with 6DC-to-DOA ratios larger than 1, an open-porous ladder pattern is realized, where the excess 6DC not bound to DOA acts as spacers between the bimolecular chains. Recently, we have shown that this specific network and its hierarchic energetics can be exploited to induce thermally activated molecular diffusion, guided in one dimension.<sup>55</sup> At an even stoichiometric ratio, a dense-packed phase with minimal pore size was observed. Here, the spacing of 6DC–DOA chains is dictated only by steric hindrance. For ratios with higher DOA fractions,

**Received:** February 7, 2012

**Revised:** June 28, 2012

74 networks with DOA nanowire segments and 6DC spacer units  
75 occur.

76 The experimental findings are further analyzed utilizing first  
77 principle calculations for the binding energies of the identified  
78 supramolecular motifs. The modeling details the different  
79 interactions contributing to the binding motifs and explores the  
80 influence of the commensurability with the substrate.  
81 Furthermore, the calculations highlight a cooperative binding  
82 energy enhancement which plays a decisive role for the  
83 expression of the superstructures. The combination of these  
84 aspects unravels the underlying principles of the hierarchic  
85 assembly.

## 86 ■ METHODS

87 STM measurements were performed using a home-built LT-  
88 STM<sup>56,57</sup> in UHV ( $3 \times 10^{-11}$  mbar base pressure). The  
89 Ag(111) surface was prepared by repeated cycles of Ar<sup>+</sup>  
90 sputtering (flux  $\approx 7(\mu\text{A}/\text{cm}^2)$ ) and annealing to 740 K, to  
91 obtain atomically flat terraces separated by monatomic steps.  
92 Molecules were deposited from two quartz crucibles in an  
93 organic molecular beam epitaxy (OMBE) source at 379 and  
94 585 K for DOA and 6DC, respectively, whereas the substrate  
95 was held at room temperature (RT). STM data were acquired  
96 in the constant current mode with sample bias  $V_b$  as indicated  
97 and at temperatures below 14 K.

98 Adsorption models for the different network geometries were  
99 constructed by positioning ball-and-stick models of the  
100 molecular constituents on a model of the hexagonal Ag(111)  
101 lattice. The length of the molecule models was extracted from  
102 gas phase simulations, yielding 1.17 and 2.96 nm for DOA and  
103 6DC, respectively (Figure 1). The lattice constant for the  
104 substrate is 2.89 Å, and the lattice orientation of the underlying  
105 substrate was determined repeatedly by atomically resolved  
106 STM measurements. It can be assumed to be constant  
107 throughout all experiments conducted on the same single  
108 crystal. Relative positions and orientations of the molecular  
109 building blocks were extracted from different experiments for  
110 each phase. In a first step the orientation of the 6DC–DOA  
111 chains was determined relative to the substrate high-symmetry  
112 directions, followed by positioning the nitrogen atoms of the  
113 end groups over hollow sites of the substrate as was established  
114 in a previous study.<sup>58</sup> Thereby, the periodicity of the assembly  
115 and the exact position of the molecules and their functional  
116 units relative to each another was determined and finally  
117 compared to experimental data for all assemblies.

118 For the theoretic analysis we employed the density functional  
119 theory framework, within the projector augmented-wave  
120 approach and the local density approximation on exchange–  
121 correlation energy, as implemented in the Abinit code.<sup>59,60</sup>  
122 Calculations taking into account the substrate are extremely  
123 demanding regarding computational resources for the large unit  
124 cells of the molecule networks presented here. Therefore, the  
125 simulations for the binding energies were conducted in an  
126 adlayer focused approach imposing a 2D-confinement to the  
127 structures<sup>61</sup> but neglecting the Ag surface. To justify this  
128 approach, the impact of the substrate on the binding properties  
129 was investigated in a smaller model system, namely HCN and  
130 benzene. When the distance dependent intermolecular  
131 interaction energy is computed with and without a Ag-layer  
132 being present, we find an increase in binding energy by  $\sim 10\%$   
133 and a reduced binding distance by 4% in the presence of the  
134 surface. In addition, the light exchange–correlation functionals  
135 used in the simulations poorly reproduce the van der Waals

136 interactions between molecules and substrate, introducing an  
137 additional source of uncertainty. Therefore, we conclude that  
138 even with the neglected substrate our approach is useful for the  
139 comparison of the relative interaction energies for the  
140 individual binding motifs.

141 All binding energies were calculated with periodic boundary  
142 conditions. To extract the binding between a pair of molecules,  
143 the distance to the next pair was increased  $>10$  Å. In a first step,  
144 the interactions between individual pairs of molecules was  
145 probed by relaxing the pair geometry with the only restriction  
146 being that N and O atoms are fixed in the (*xy*) plane (as was  
147 previously determined in related NEXAFS studies<sup>62,63</sup>), thereby  
148 defining a 2D environment. To specifically account for the  
149 substrate influence and different relative positions observed in  
150 the experiment, molecules were restrained to the positions  
151 determined from STM data with flat geometries; i.e., the  
152 substrate acts as a position-selective filter.

153 For an analysis of the different contributions of the individual  
154 interactions to the total binding energy of the complex 6DC–  
155 DOA binding motif, we performed calculations where the  
156 carbonitrile moiety was replaced by a hydrogen atom. This way,  
157 the interacting energy of the DOA functional unit with the  
158 6DC phenyl ring could be quantified. The difference in binding  
159 energy between the calculations with and without CN group is  
160 attributed to the presence of the CN $\cdots$ HN and CN $\cdots$ phenyl  
161 bonds and can finally be deconvoluted. For further details on  
162 the employed computation method, also see ref 55.

## 163 ■ RESULTS AND DISCUSSION

164 **STM Observations.** The pure phases of the DOA and 6DC  
165 molecular building blocks employed (cf. Figure 1) have been  
166 investigated previously.<sup>58,62,64</sup> It was shown that templates  
167 engineered with these moieties can be utilized as host lattices to  
168 confine supramolecular rotors,<sup>29</sup> to control surface electronic  
169 states in arrays of quantum dots,<sup>65,66</sup> or to steer the adsorption  
170 of single metal atoms<sup>67</sup> and clusters.<sup>68</sup>

171 Structure models of the molecules are illustrated in Figure 1.  
172 DOA consists of two amide groups interrelated by a  $\sigma$  C–C  
173 bond with a phenyl group attached on each nitrogen atom of  
174 the functional unit. In the pure phase DOA is known to form  
175 nanogratings or a dense phase respectively, where the binding is  
176 mediated via the central amide groups. The formation of pairs  
177 in the submonolayer regime is attributed to adsorption in  
178 registry with the Ag(111) surface and was shown to disappear  
179 at monolayer coverage.<sup>67</sup> Due to the symmetry breaking  
180 presence of the substrate the molecule is found in two  
181 enantiomeric configurations. 6DC features six phenyl rings in  
182 linear arrangement bonded by  $\sigma$  C–C bonds and terminated on  
183 either end with a carbonitrile group. 6DC network formation in  
184 the pure phase is driven by the interaction of the carbonitrile  
185 moieties with the aromatic rings of adjoining molecules yielding  
186 a 4-fold nodal motif.<sup>58</sup> The homobonded networks feature  
187 several geometries depending on molecule coverage, whereas  
188 metal–organic honeycomb nanomeshes are formed exclusively  
189 following cobalt exposure.<sup>69</sup>

190 In STM the molecular brick DOA appears as double  
191 protrusions connected by a thinner waist, whereas 6DC is  
192 resolved as longer, rodlike features (Figure 1a–d, DOA and  
193 6DC, respectively, symbolized as green and yellow bricks in the  
194 following). When both molecules are codeposited on the  
195 Ag(111) metal surface at RT and cooled to liquid helium  
196 temperature, new networks evolve (Figure 1a–c). Four  
197 different molecule–molecule interactions are present in the

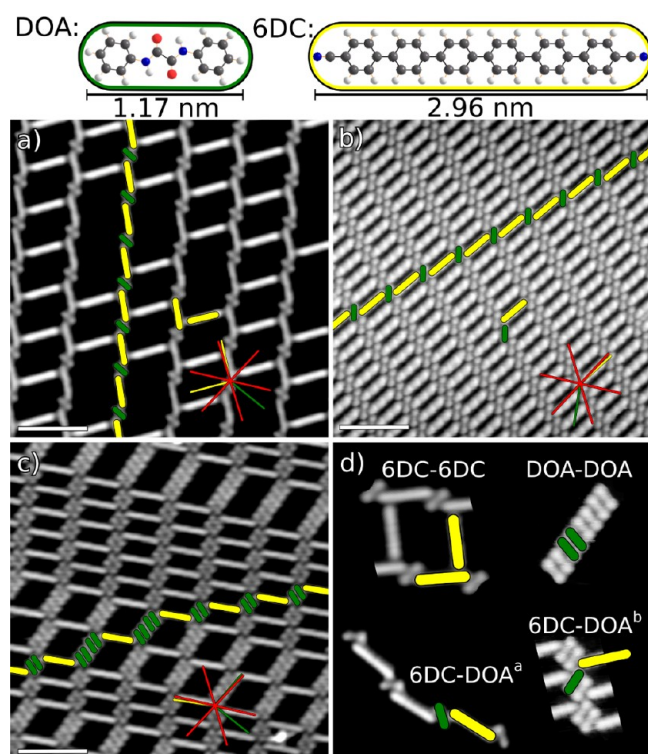


**Figure 1.** Top: structure models of the molecules with their respective lengths (H, white; C, black; O, red; N, blue). (a)–(c) Different regular network types depending on the stoichiometric ratios  $S$ . DOA and 6DC are indicated by green and yellow bricks, respectively. The relative orientation of the different molecules in the networks with respect to the high-symmetry directions (red) of the Ag(111) substrate are indicated in the bottom right part. Scale bars  $\approx 5$  nm. (a) Open porous phase with  $S = 2$  establishing a ladder-shaped geometry.  $I_T = 76$  pA,  $V_B = 0.2$  V. (b) At even ratio  $S = 1$  no spacers are present and the lines are dense-packed maintaining their original directionality.  $I_T = 68$  pA,  $V_B = 0.8$  V. (c) With increasing DOA concentration ( $S = 1/2$ – $1/6$ ) open-porous arrangements are formed where pairs of DOA interconnecting the 6DC–DOA planes define the exact geometry.  $I_T = 72$  pA,  $V_B = -1$  V. (d) Schematic of the elementary binding motifs observed in the entirety of networks.

total set of superstructures (Figure 1d), namely the two binding motifs connecting identical constituents (6DC–6DC and DOA–DOA), thus featuring homobonding, and two heterobonding motifs (6DC–DOA<sup>a</sup> and 6DC–DOA<sup>b</sup>) connecting the two species. The 6DC–DOA<sup>a</sup> motif is the only one present in all mixed assemblies, indicating that this is the prevailing interaction. Clearly, open-porous bicomponent networks with dominant heterobonding are preferred over phase segregation into islands of single species where only homobonding is possible. The emerging geometries of the supramolecular arrangements depend on the stoichiometric ratio  $S$  being defined as the number of 6DC molecules divided by the number of DOA molecules. For  $S = 1$  only heterobonding interactions are present (Figure 1b), whereas at  $S \neq 1$  homobonding of either species reappears (Figure 1a,c).

For excess 6DC ( $S > 1$ ), a ladder-shaped network is observed (Figure 1a) in which 6DC acts as runglie spacers between 6DC–DOA chains. From a detailed analysis and modeling, it was established that the molecular backbone of the 6DC units in the mixed chains encloses an angle of  $1.6^\circ$  with the high-symmetry directions of the substrate (red star, orientations of the molecules shown by yellow and green lines).<sup>55</sup> Rungs

connect to the head of these 6DC units under  $\sim 83^\circ$ . For the ideal 2:1 stoichiometry, where linkers are present at every possible head position between the 6DC–DOA lines, this phase features pores with a van der Waals area of  $\approx 7$  nm<sup>2</sup>. In a previous study<sup>55</sup> we demonstrated that the bimolecular chains are stronger bound than the rungs and thus can be utilized to guide the thermally activated one-dimensional diffusion of 6DC in between.

At  $S = 1$  and sufficiently high total coverage a dense phase of 6DC–DOA chains is observed (Figure 1b), where exclusively 6DC–DOA interactions are present (cf. 6DC–DOA<sup>a</sup> and 6DC–DOA<sup>b</sup> in Figure 1d). Averaged over the entire surface this sample actually exhibited a slight excess of 6DC. We found that the binary phase covered most of the terraces, whereas a minority of terraces partially filled exclusively with 6DC existed. This marks a first indication that heterobonding is thermodynamically preferred.

When the relative amount of DOA is increased ( $S < 1$ ), the formation of DOA-chain segments connecting 6DC lines is observed (Figure 1c). Instead of single DOA molecules with one 6DC binding on either side to the functional unit, now we encounter pairs and multiples thereof in between the 6DC lines. We therefore conclude that the pair formation in the investigated bicomponent networks follow closely the assembly principles identified for molecular nanogratings formed in the case of pure DOA.<sup>62,67</sup> The van der Waals pore sizes in this network type consequently increases from  $\approx 2$  nm<sup>2</sup> for two DOA spacers up to  $\approx 7$  nm<sup>2</sup> for six spacers. Importantly, the average pore size of these mixed networks can be controlled via the DOA concentration.

For a better understanding of the underlying assembly principle, we address structure formation on a larger scale and for extreme cases of coverage and stoichiometric excess. For all types of arrangements it was found that the symmetry of the substrate was reflected in the epitaxy, giving rise to three orientational domains (rotated by  $120^\circ$ ) for each handedness (right or left) as illustrated in Figure 2a–c. The handedness of the resulting structures is triggered by the two enantiomers of DOA, where 6DC either connects toward the right or left side of DOA along the 6DC–DOA chain directions (cf. Figure 1d). This leads to a rotation of the chains away from the high-symmetry directions of the substrate. In Figure 2a, the different domain orientations of the ladder shaped network ( $S = 2$ ) are indicated along with the related handedness.

For very small relative amounts of 6DC ( $S \approx 0.1$ , Figure 2b) chains of DOA evolve, again exhibiting different handedness. 6DC then merely interconnects DOA chains, leading to staircase-like structures (highlighted in green and yellow) lacking long-range order.

In the case of  $S = 1$ , but with an extremely low total coverage, mainly 6DC–DOA chaining occurs (Figure 2c) with very limited expression of regular ladder structures. The chain segments follow the different surface directions similar to the long-range ordered bimolecular networks described above but show chirality interconversion along the assembly direction, which explains their meandering. Without spatial restrictions the 6DC–DOA<sup>a</sup> interaction is preferred over the three other binding motifs.

From the sum of the data we can conclude the following: (i) All structures appear with a strict directionality as well as chiral properties. Together with the consequent absence of Moiré patterns, this is evidence that the observed arrangements are commensurate with the underlying Ag(111) substrate and that

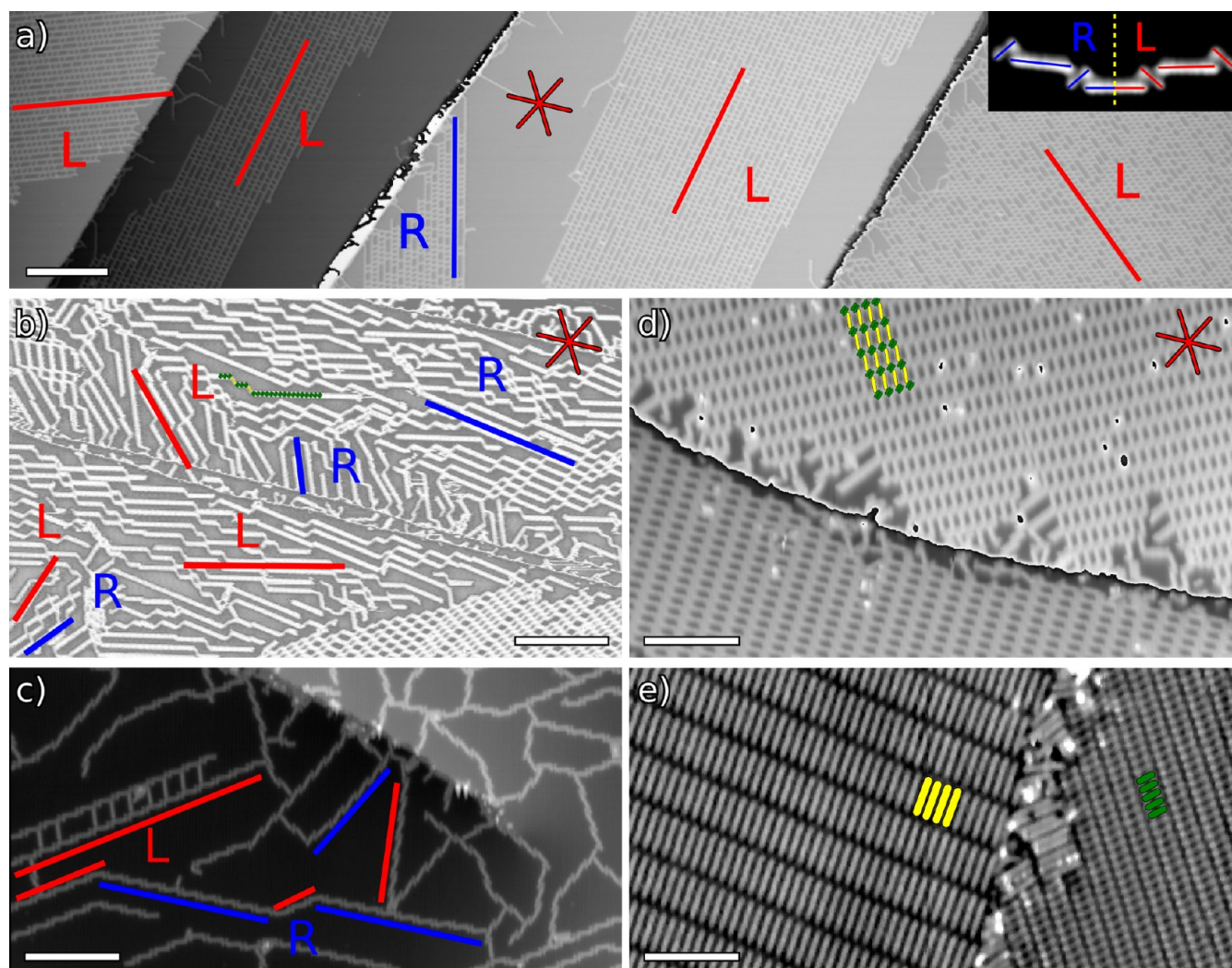


**Figure 2.** Mesoscopic order of of different networks arising at different 6DC:DOA stoichiometries. Right and left handedness of the domains are marked by blue R and red L, respectively; for definitions see the inset in (a). High-symmetry directions of the substrate are indicated with red stars. (a) Open porous 2:1 phase. The observation of different directions related to the high-symmetry directions and different handedness suggest commensurate ordering.  $I_T = 76$  pA,  $V_B = -0.6$  V, scale bar = 50 nm. (b) Different directional arrangements and handedness of DOA lines interconnected by single 6DC are observed in samples with high DOA concentration.  $I_T = 78$  pA,  $V_B = -0.7$  V, scale bar = 30 nm (c) For low coverages no long-range ordered networks evolve, but rather short chains of 6DC–DOA also showing chirality interconversion.  $I_T = 63$  pA,  $V_B = -1.2$  V, scale bar = 12 nm (d) Sample with 6DC:DOA close to 1:2 ratio demonstrates the preference of 6DC–DOA chaining over pure 6DC–6DC and DOA–DOA motifs.  $I_T = 66$  pA,  $V_B = 0.8$  V, scale bar = 15 nm. (e) Upon postdeposition of 6DC onto a full monolayer of DOA, the fractional DOA coverage is reduced and dense-packed networks as in the pure phase of each constituent.  $I_T = 84$  pA,  $V_B = -1.4$  V, scale bar = 6 nm.

283 the local epitaxies of the different binding motifs are very  
 284 similar independent of the assembly into which they are  
 285 incorporated. (ii) The self-assembly process incorporates  
 286 hierarchic principles. At every given stoichiometry  $S$ , the  
 287 heteromolecular 6DC–DOA<sup>a</sup> bonding is established, with  
 288 excess molecules forming homobonds determining the exact  
 289 arrangement. (iii) For the expression of *regular* networks an  
 290 appropriate total coverage is required. This is further  
 291 exemplified in Figure 2d where for  $S = 1/2$ , long-range ordered  
 292 domains are formed. This demonstrates that with the  
 293 appropriate control over stoichiometry and coverage the quality  
 294 of the supramolecular architecture can be increased over the  
 295 case displayed in Figure 1c, where the pore-size shows a  
 296 broader distribution.

297 An additional experiment was carried out testing the  
 298 correlation of phase segregation with spatial restrictions. First,  
 299 a saturated monolayer of DOA was deposited onto the Ag(111)

surface. Then, while the substrate was kept at RT,  $\sim 0.5$  300  
 monolayers of 6DC was subsequently deposited onto the 301  
 preassembled DOA layer. After cooling (Figure 2e), regular 302  
 dense-packed domains of either constituent are separated by 303  
 irregular boundaries often following step edges. Thus 6DC 304  
 arriving at the surface can replace DOA molecules in the first 305  
 adsorbate layer and form dense-packed islands surrounded by 306  
 DOA. Having been pushed to the second layer, the DOA units 307  
 desorb, because at RT the interlayer attraction is too weak to 308  
 stabilize the second layer, which was established in a previous 309  
 work.<sup>67</sup> We conclude that phase segregation is only decisive 310  
 when very high total coverage produces strong spatial 311  
 limitations that prevent the emergence of bimolecular 312  
 structures which all feature porosity and have lower density. 313

**Network Analysis.** To gain further insight into the different 314  
 interactions between the molecular constituents, a precise 315  
 description of the superstructures is necessary. Therefore, we 316

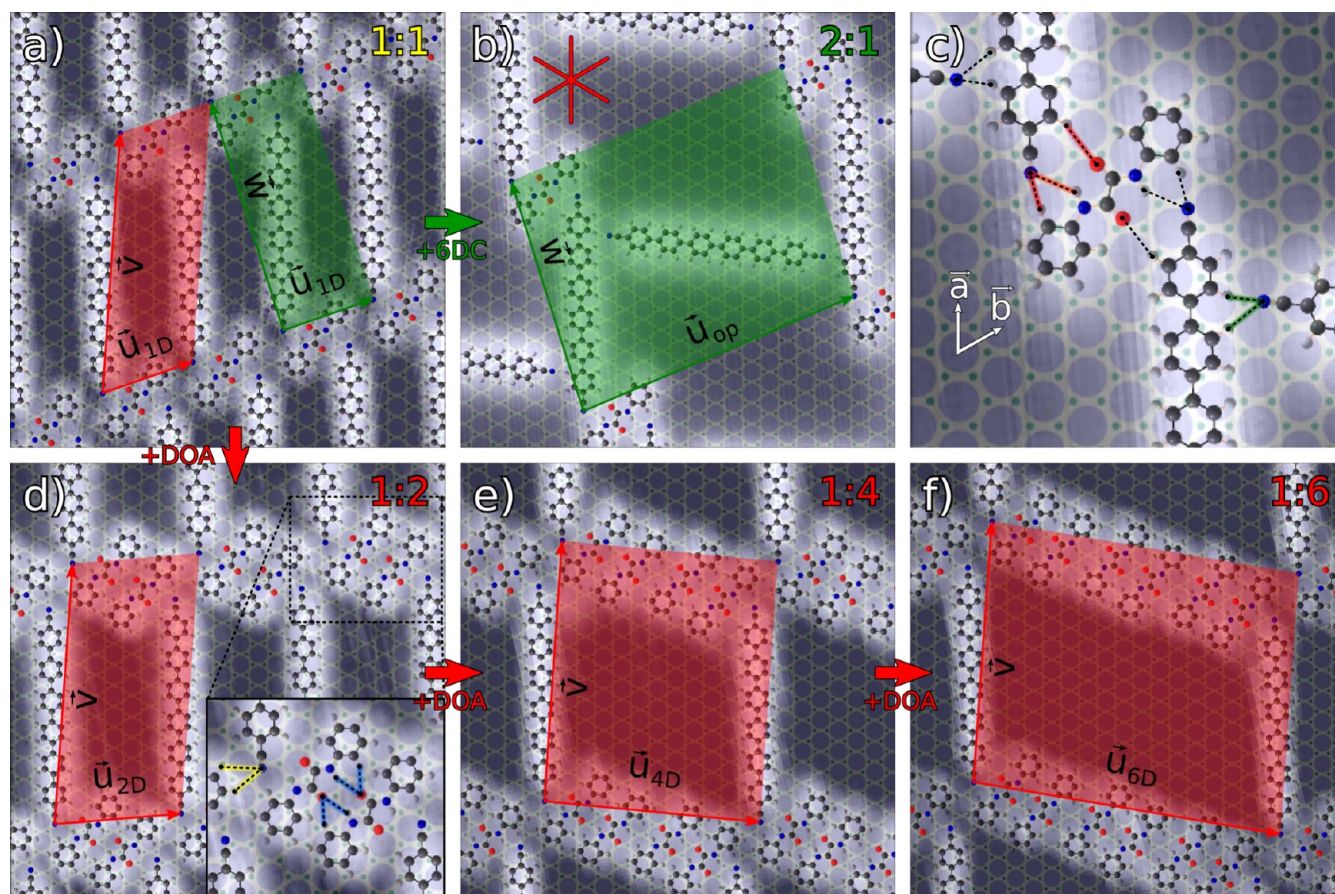


**Figure 3.** Structure models for networks at different stoichiometry. The molecular models and the Ag(111) lattice are superimposed onto experimental data (white). Unit cells are indicated in red and green. (a) Dense packed  $S = 1$  phase with elementary unit cells identified as basis for all other assemblies. (b) Open porous phase with 6DC:DOA ratio  $S = 2$ . (d)–(f) Increasing DOA concentration from  $S = 1/2$  to  $S = 1/6$  shows a systematic increase of pore size while the direction of the 6DC–DOA chains is maintained. (c) Close-up model showing the geometries of the 6DC–DOA<sup>a</sup> (green) and the 6DC–6DC (blue) interaction. The inset in (c) displays the DOA–DOA (blue) and 6DC–DOA<sup>b</sup> (yellow) interaction. For the matrix notation of the unit cells  $\vec{a}$  and  $\vec{b}$  are used for the substrate lattice vectors.

317 inspected and modeled the regular arrangements in detail,  
 318 posing the condition of commensurability based on the above-  
 319 mentioned reasoning. The orientation of the substrate and the  
 320 calibration of the piezo constants were checked repeatedly by  
 321 atomically resolving the substrate. The alignment of the  
 322 individual molecules relative to the high-symmetry directions  
 323 of the substrate and the periodicities in the specific network  
 324 directions were determined on different days and averaged. The  
 325 redundancy introduced by rotated variants of the same  
 326 superstructure as well as the simultaneous imaging of right-  
 327 and left-handed domains help to minimize the error of the  
 328 obtained values. All models not only fit experimental data  
 329 locally but also fit data for extended areas with a maximum  
 330 deviation of  $2^\circ$  for directions and 4% for lengths. In our  
 331 previous work with 6DC<sup>29,58</sup> we found that its aromatic  
 332 backbone is predominantly aligned along  $\langle 1\bar{1}0 \rangle$  and  $\langle 1\bar{1}2 \rangle$  and  
 333 that the nitrogen atoms are accommodated near hollow sites.  
 334 All models presented here are consistent with these principles  
 335 and thus we are confident that also the epitaxy with the metal  
 336 surface is well described even though the simultaneous imaging  
 337 of adsorbates and atomically resolved substrate was not  
 338 obtained.

339 The proposed geometries are displayed in Figure 3, where  
 340 ball-and-stick models of the adsorbates and the first substrate  
 341 layer (gray circles, hollow sites indicated by green dots) are

superimposed onto STM images presenting the molecules in 342  
 white. For simplicity, only planar conformations are used for 343  
 both 6DC and DOA obtained by appropriate geometric 344  
 restraints during DFT optimization of isolated entities. Unit 345  
 cell vectors are indicated by red or green arrows. 346

The  $S = 1$  phase (Figure 3a) is assembled from chains of 347  
 alternating 6DC and DOA along  $\vec{W}$ , as already highlighted in 348  
 Figure 1b. 349

The chains form an array through being laterally offset by 350  
 $\vec{U}_{1D}$ , resulting in the green unit cell. This network can 351  
 alternatively be described by the red unit cell, in which  $\vec{W}$  is 352  
 replaced by  $\vec{V}$ . With the substrate lattice vectors  $\vec{a}$  and  $\vec{b}$  (Figure 353  
 3), the matrix notation for the unit cells yields 354

$$\begin{pmatrix} \vec{W} \\ \vec{U}_{1D} \end{pmatrix} = \begin{pmatrix} 11\vec{a} - 4\vec{b} \\ 5\vec{b} - \vec{a} \end{pmatrix} \quad \text{and} \quad \begin{pmatrix} \vec{V} \\ \vec{U}_{1D} \end{pmatrix} = \begin{pmatrix} 12\vec{a} + \vec{b} \\ 5\vec{b} - \vec{a} \end{pmatrix}$$

The two unit cells are important for understanding the relation 355  
 between the phases with different stoichiometric ratios. 356  
 Superstructures with  $S \geq 1$  (green unit cells) feature the 357  
 same  $\vec{W}$ , but varying  $\vec{U}$ . Supramolecular arrangements with  $S \leq$  358  
 1 comprise a constant  $\vec{V}$  and a systematically increasing  $\vec{U}_{nD}$  359  
 (Figure 3a,d,e,f). 360

In the ladder-shaped  $S = 2$  phase, 6DC molecules act as 361  
 spacers between the bimolecular chains increasing the lateral 362

363 offset. Therefore, the unit cell (green) contains one DOA and  
364 two 6DC and is given in matrix notation by

$$\begin{pmatrix} \vec{W} \\ \vec{U}_{op} \end{pmatrix} = \begin{pmatrix} 11\vec{a} - 4\vec{b} \\ 15\vec{b} - 2\vec{a} \end{pmatrix}$$

365 Figure 3c highlights two of the four molecule–molecule  
366 interactions present in the total set of networks, namely the  
367 tridentate 6DC–DOA<sup>a</sup> (red) and the bidentate 6DC–6DC  
368 interaction (green). At higher DOA concentrations ( $S < 1$ ) the  
369 DOA–DOA interaction (blue) is present (cf. inset in Figure  
370 3d) manifested in a tetradentate fashion. The DOA pairs  
371 consist of enantiomers of the same handedness. This  
372 contravenes with the racemic mixture proposed in previous  
373 work.<sup>64</sup> Both the symmetry of the supramolecular arrangements  
374 found here and our much broader theoretic analysis carried out  
375 now strongly corroborate that the pairs are actually  
376 enantiopure. Figure 3d also details the 6DC–DOA<sup>b</sup> interaction  
377 (yellow) which is also encountered for  $S = 1$ .

378 The unit cells of the networks presented in Figure 3d–f,  
379 comprise one 6DC and two, four, or six DOAs, respectively.  
380 The vector  $\vec{U}_{nD}$ , where  $n$  is the number of DOA molecules,  
381 increases by  $\Delta = 5\vec{b} - 4\vec{a}$  for each supplementary DOA pair.  
382 With  $n = 2, 4, 6$  the three unit cells can be summarized by

$$\begin{pmatrix} \vec{v} \\ \vec{U}_{nD} \end{pmatrix} = \begin{pmatrix} 12\vec{a} + \vec{b} \\ 2\vec{b} + 1\vec{a} + \frac{n}{2}\Delta \end{pmatrix}$$

383 **Modeling of Bond Motifs.** To understand the origin of the  
384 observed hierarchic organization, we employed a three-step  
385 approach. First, we characterized the different binding motifs  
386 without any additional influence. For this we calculated the  
387 energy-optimized geometries by a full relaxation of the involved  
388 molecules yielding the maximum possible binding energy for  
389 each intermolecular interaction. Second, we address the  
390 influence of the substrate by imposing molecular conformations  
391 and intermolecular distances according to the findings of the  
392 network analysis. This step results in a reduction of the binding  
393 energies of all motifs consistent with the enlargement of the  
394 binding distances forced by the substrate commensurability.  
395 Finally, we investigate the changes resulting from incorporating  
396 the motifs into periodic structures yielding mainly cooperativity  
397 effects.

398 For the modeling of the 6DC–6DC interaction (green),  
399 diphenyl dicarbonitrile (2DC), and quarterphenyl dicarbonitrile  
400 (4DC) were used (Figure 4a) to reduce computation time.  
401 This has shown to have only little effect on the calculated  
402 binding energy compared to using 6DC, see ref 55. After full  
403 relaxation, the binding energy amounts to  $-220$  meV for  
404 binding under  $90^\circ$ . The equilibrium distance between the  
405 binding N atom and the nearest H atoms is close to  $2.4$  Å.  
406 Strictly speaking, this interaction is not a bidentate, weak H-  
407 bond, rather the full phenyl rings of the 4DC are involved,  
408 which will be discussed in an upcoming publication.

409 After the DOA–DOA motif (Figure 4b, blue) fully relaxes,  
410 the DOA molecules exhibit a notable bending and tilting of the  
411 phenyl rings. The attraction is mediated by two  $\text{CO}\cdots\text{HN}$   
412 hydrogen bonds with a  $\text{O}\cdots\text{H}$  binding distance of  $1.8$  Å. The  
413 steric hindrance between phenyl rings causes the tilting of the  
414 phenyl moieties by  $23^\circ$  as visible in the side view. The second  
415 molecule is offset with respect to the first by  $5.0$  Å. The binding  
416 energy amounts to  $-655$  meV.

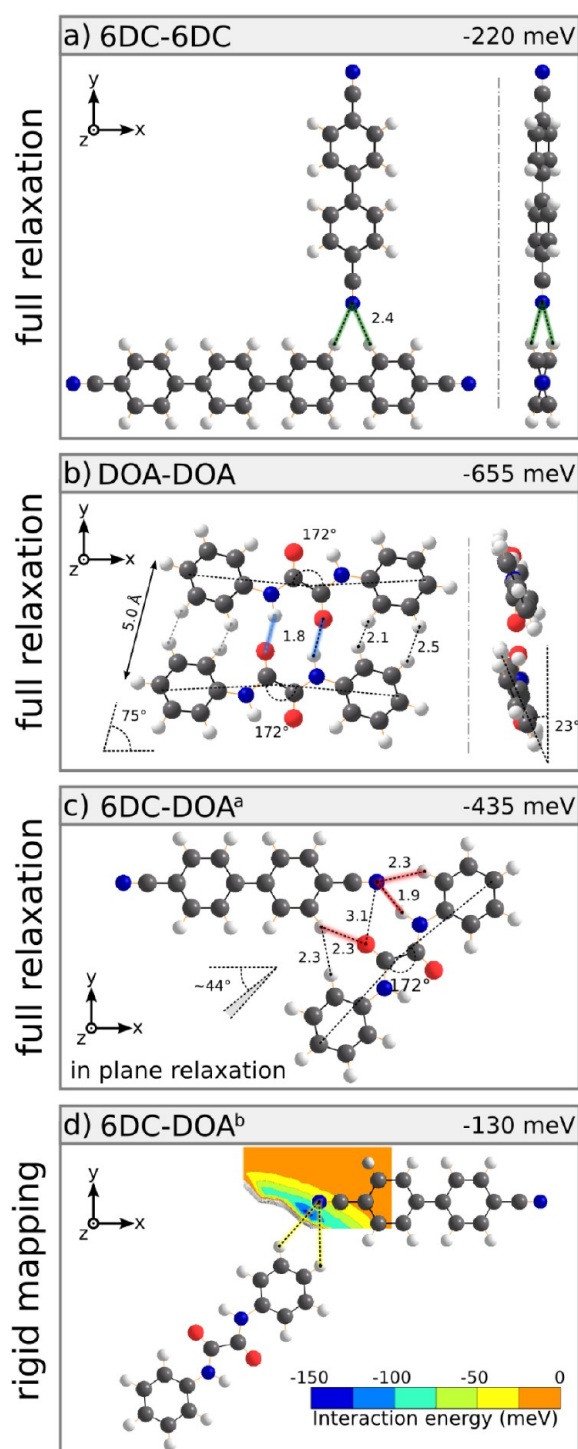


**Figure 4.** Computed geometries and energies for the intermolecular interactions. Interatomic distances (Å) and angles (deg) are given for the fully relaxed geometry along with side views when rotated phenyl rings result. The binding energy for the relaxed geometry is indicated. The N atoms in (a) and the amide groups in (b) are restricted to the ( $xy$ ) plane, whereas in (c) the entire geometry was fully relaxed without boundary conditions. (d) Energy map obtained by rigidly displacing the 2DC molecule around the experimentally observed position for flat molecule geometries.

Using 2DC–DOA<sup>a</sup> as a model for the 6DC–DOA<sup>a</sup> 417 interaction (Figure 4c, red), the full relaxation yields a binding 418 energy of  $-435$  meV and an angle of  $44^\circ$  between the two 419 molecules. The attraction is a result of one  $\text{N}\cdots\text{HN}$  hydrogen 420

421 bond and two weak interactions again involving the phenyl  
422 rings similar to the 6DC–6DC and DOA–DOA cases. As  
423 detailed in the Methods, the three contributions to the binding  
424 energy were evaluated to be  $\approx 50\%$  for the CN $\cdots$ HN bond and  
425  $\approx 30\%$  for the CN $\cdots$ phenyl and  $\approx 20\%$  for the CO $\cdots$ phenyl  
426 interactions, respectively. The DOA unit exhibits a slight  
427 distortion of the long molecular axis ( $172^\circ$ ).

428 Finally, the 6DC–DOA<sup>b</sup> interaction (Figure 4d, yellow) is  
429 assessed. In this case a full geometric relaxation was not carried  
430 out because it ultimately leads to the 6DC–DOA<sup>a</sup> motif.  
431 Therefore, we defined a relative orientation of a planar 2DC  
432 with respect to a planar DOA species according to the  
433 experimental findings and mapped the interaction energy  
434 landscape via rigidly displacing one against the other yielding a  
435 minimum of  $-130$  meV.

436 Comparing the relative strengths of the four pairwise  
437 molecule–molecule interactions cannot explain the preference  
438 for assembling 6DC–DOA chains in the case of  $S = 1$ . Because  
439 establishing two 6DC–DOA<sup>a</sup> motifs results in the same energy  
440 gain ( $-870$  meV) as one DOA–DOA and one 6DC–6DC  
441 ( $-875$  meV), from the energetics one would expect the  
442 unordered manifestation of combinations of these motifs rather  
443 than the sole appearance of chains (cf. Figure 2c). However, it  
444 is obvious that the relaxed geometries of the linked pairs deviate  
445 strongly from the experimental observations (cf. Table 1).  
446 Therefore, in the second step of our theoretical analysis we  
447 calculated the binding energies for molecular geometries  
448 according to the experimental findings.

**Table 1. Relevant Angles and Distances for Molecule Interactions Extracted from STM Data and the Fully Relaxed Geometries, Respectively**

quantity	STM observation	relaxed geometry
$\angle 6DC-6DC$ , deg	82.8	90
$6DC-6DC$ (N $\cdots$ H), Å	2.2/2.7	2.4
$\angle 6DC-DOA$ , deg	44	44
$6DC-DOA$ (N $\cdots$ H), Å	2.9	1.9
$\angle DOA-DOA$ , deg	78	75
$DOA-DOA$ (O $\cdots$ H), Å	2.6	1.8

449 The main differences between the relaxed (Figure 4) and the  
450 experimental (Figure 3) geometries are longer distances  
451 between the constituents as a result of the commensurability  
452 with the substrate and straight DOA units due to attractive  
453 forces from both sides instead of one side only. These effects  
454 lead to a decrease of the binding energy in all cases (Table 2).  
455 The greatest impact is found for the DOA–DOA motif. The  
456 offset between the DOA moieties is increased by  $\sim 1$  Å (Table  
457 1). Furthermore, the interaction is now mediated via two

**Table 2. Binding Energies (meV) of the Intermolecular Interactions Contributing to the Bimolecular Networks<sup>a</sup>**

binding motif	relaxed geometry	experimental geometry	superstructure
6DC–DOA <sup>a</sup>	$-435$	$-250$	$-295$
DOA–DOA	$-655$	$-310$	$-255$
6DC–6DC	$-220$	$-185$	$(-185)$
6DC–DOA <sup>b</sup>	$-130$	$-70$	$-60$

<sup>a</sup>The different columns compare geometries obtained by unrestricted relaxation (where possible), from the experimental findings and taking into account superstructure boundary conditions.

O $\cdots$ phenyl attractions in addition to the two weakened O $\cdots$ HN  
458 hydrogen bonds (cf. Figure 3d). As a result, the phenyl rings  
459 are no longer tilted. The binding energy of a single DOA pair  
460 markedly reduces to  $-310$  meV.

461 With the energies obtained in the second step, the 6DC–  
462 DOA chains ( $-500$  meV) are not the structure hierarchically  
463 dominating over pairs of DOA and 6DC ( $-495$  meV). Since so  
464 far our reasoning was based on formation energetics of isolated  
465 pairs, we further refined our modeling by extending the  
466 simulations to using 6DC instead of 2DC and including  
467 periodic boundary conditions (Figure 5).  
468

469 For simulating periodic chains of the 6DC–DOA<sup>a</sup> motif, we  
470 fixed the geometry of the two molecules to the experimental  
471 values (highlighted in red in Figure 5a) and positioned a  
472 periodic image with an offset  $X$ . We find that the binding  
473 energy for bond N<sup>o</sup>1 is increased from  $-250$  to  $-265$  meV by  
474 using 6DC instead of 2DC. Furthermore, we compare the total  
475 binding energy of two adjacent bonds in a 6DC–DOA<sup>a</sup> chain  
476 (bond N<sup>o</sup>1 + bond N<sup>o</sup>2) to the sum of two individual 6DC–  
477 DOA<sup>a</sup> bonds. The offset-dependent interaction energy curve  
478 shows a minimum in which the energy is lower than  $-600$   
479 meV. At the nearest position allowed by the substrate  
480 commensurability, which was defined as  $X = 0$ , the energy  
481 amounts to  $-590$  meV and is  $60$  meV lower than for the two  
482 isolated bonds. Thus, per intermolecular interaction a  
483 cooperative effect of  $\approx 30$  meV stabilizes the periodic structure  
484 leading to an increase in binding energy from  $-265$  to  $-295$   
485 meV.

486 Next, we address the DOA–DOA chain formation. As visible  
487 in Figure 3e,f, chains are constructed of pairs of DOA units that  
488 are laterally offset with respect to the chain direction. Thus, the  
489 chains are actually held together by two different types of  
490 DOA–DOA interactions, namely the already described intra-  
491 pair variant (inset in Figure 3d, binding energy  $-310$  meV) and  
492 the interpair variant (e.g., in the center of the DOA chain in  
493 Figure 3e). Our simulation of the latter geometry (not shown)  
494 yields a binding energy of  $-200$  meV. Therefore, the average  
495 energy for DOA chains is actually reduced to  $-255$  meV per  
496 molecule when extended chaining is taken into consideration.

497 Finally, we investigate the influence of the 2D network  
498 environment on the 6DC–DOA<sup>b</sup> interaction. Therefore, we  
499 fixed a 6DC–DOA–6DC triplet in the geometry according to  
500 experimental findings (Figure 5b, red) and placed a periodic  
501 image with an offset  $\bar{X}$ . The interaction energy landscape was  
502 then mapped by changing  $\bar{X}$  in the area displayed in Figure 5b.  
503 With the interaction energy in the experimental geometry being  
504  $-60$  meV, there seems to be almost no cooperative effect, and  
505 the replacement of the 2DC by a 6DC does not significantly  
506 alter the situation. The map of the interaction energy is,  
507 however, very instructive, as it reveals the frustration of the  
508 experimental configuration, forced by the substrate periodicity,  
509 despite a complex energy landscape of the laterally interacting  
510 6DC–DOA chains.

511 After inclusion of the periodic environments into our  
512 modeling, the experimentally observed hierarchy of the  
513 different interactions can be understood with the respective  
514 energetics (Table 2). In superstructures with  $S = 1$  the sole  
515 manifestation of heterobonding 6DC–DOA<sup>a</sup> interactions  
516 (average binding energy of  $-295$  meV per motif) is  
517 energetically preferred over establishing homobonding DOA–  
518 DOA and 6DC–6DC interactions ( $0.5(-255-185) = -220$   
519 meV per motif). The latter energy only in cases with  $S \neq 1$ .  
520 The smallest energy gain results from 6DC–DOA<sup>b</sup> con-

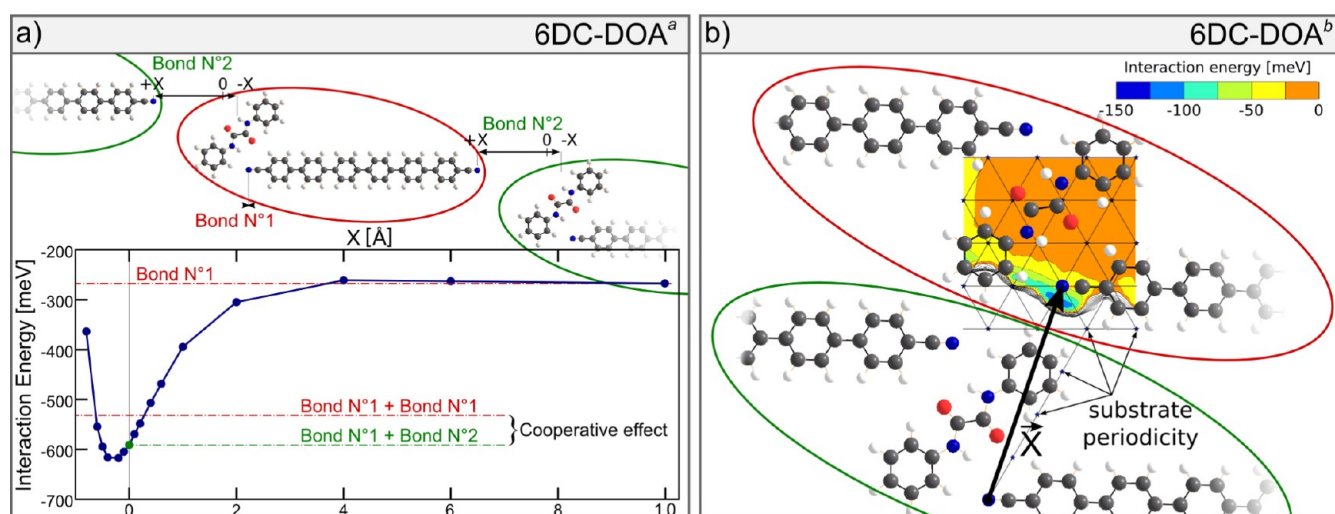


**Figure 5.** Computation of the cooperative effect on 6DC–DOA interactions. (a) 6DC–DOA<sup>a</sup>. Energy curve obtained by rigidly displacing the 6DC–DOA pairs with respect to one another.  $X$  (Å) is thereby the displacement between the nitrogen atom of 6DC and the hydrogen atom of the top functional group of DOA forming the stronger  $\alpha$  bond. When two 6DC molecules are bonded to one DOA molecule (in the observed configuration), a total cooperative energy of  $-60$  meV is obtained. (b) 6DC–DOA<sup>b</sup>. Energy map obtained by rigidly displacing the 6DC–DOA chains with respect to one another. The cooperative effect is minimal. The difference in energy mainly arises from the change of molecule from 2DC to 6DC.

521 nections, which are too weak to force the formation of dense  
522 islands (Figure 1b) if the total coverage is not high enough  
523 (Figure 2c).

## 524 ■ CONCLUSION

525 In conclusion, we investigated the hierarchic self-assembly of  
526 bicomponent organic molecular networks constructed with  
527 6DC and DOA on the smooth Ag(111) surface and analyzed  
528 the emergence of network types formed at different  
529 stoichiometric ratios. The geometry and alignment of all  
530 regular phases was determined. The preferred formation of  
531 6DC–DOA chains found in the experiment could be  
532 rationalized through theoretically investigating the different  
533 characteristics of the identified intermolecular interactions  
534 taking into account the influence of the substrate commensur-  
535 ability and cooperative effects present in the periodic  
536 superstructures. For all given stoichiometric ratios of the two  
537 organic constituents, the same hierarchic construction  
538 principles are employed. First, as many 6DC–DOA<sup>a</sup>  
539 interactions as possible are established, followed by the excess  
540 species forming homobonds ultimately defining the network  
541 geometry. The presented model system is highly versatile as the  
542 pore size in the networks can be tuned by varying the relative  
543 amounts of the provided constituents and providing an  
544 appropriate total coverage. Due to the universal nature of the  
545 complex assembly scenario, the concepts of our work can be  
546 adapted for a large variety of surface-confined nanoarchitec-  
547 tures. For example, hierarchic protocols similar to the one  
548 presented can be extended to different substrates or increasing  
549 emphasis can be put on realizing network functionalization  
550 such as the integration of molecular switches via suitably  
551 designed molecular building blocks.

## 552 ■ AUTHOR INFORMATION

### 553 Corresponding Author

554 \*E-mail: wkrenner@ph.tum.de. Phone: +49 89 12848. Fax: +49  
555 89 12338.

## Present Addresses

556 §Institute of Electronics, Microelectronics and Nanotechnology, 557  
558 UMR CNRS 8520, Avenue Poincaré, BP 60069, 59652 559  
560 Villeneuve d'Ascq, France. 561  
562 ||PCMS-CNRS UMR 7504, University of Strasbourg, 23 Rue  
563 du Loess, 67034 Strasbourg, France. 564

## Notes

565 The authors declare no competing financial interest. 566

## ■ ACKNOWLEDGMENTS

567 Funding by the European Union via ERC Advanced Grant 568  
569 MolArt (No. 247299), the German Research Foundation 570  
571 (DFG) via BA 3395/2-1, the TUM International Graduate 572  
573 School of Science and Engineering (IGSSE) and the TUM 574  
575 Institute of Advanced Study (IAS), as well as the Alexander von 576  
577 Humboldt Foundation (Y.M.) are gratefully acknowledged. 578

## ■ REFERENCES

- 579 (1) Whitesides, G.; Mathias, J.; Seto, C. *Science* **1991**, *254*, 1312– 580  
581 1319. 582  
583 (2) Lehn, J.-M. *Makromol. Chem. - Macromol. Symp.* **1993**, *69*, 1–17. 584  
585 (3) Zhang, S. *Biotech. Adv.* **2002**, *20*, 321–339. 586  
587 (4) Barth, J. V.; Costantini, G.; Kern, K. *Nature* **2005**, *437*, 671–679. 588  
589 (5) Barth, J. V. *Annu. Rev. Phys. Chem.* **2007**, *58*, 375–407. 590  
591 (6) Liang, H.; He, Y.; Ye, Y.; Xu, X.; Cheng, F.; Sun, W.; Shao, X.; 592  
593 Wang, Y.; Li, J.; Wu, K. *Coord. Chem. Rev.* **2009**, *253*, 2959–2979. 594  
595 (7) Klyatskaya, S.; Klappenberger, F.; Schlickum, U.; Kühne, D.; 596  
597 Marschall, M.; Reichert, J.; Decker, R.; Krenner, W.; Zoppellaro, G.; 598  
599 Brune, H.; Barth, J. V.; Ruben, M. *Adv. Funct. Mater.* **2011**, *21*, 1230– 600  
601 1240. 602  
603 (8) Gimzewski, J. K.; Joachim, C.; Schlittler, R. R.; Langlais, V.; Tang, 604  
605 H.; Johansson, I. *Science* **1998**, *281*, 531–533. 606  
607 (9) van Delden, R. A.; terWiel, M. K. J.; Pollard, M. M.; Vicario, J.; 608  
609 Koumura, N.; Feringa, B. L. *Nature* **2005**, *437*, 1337–1340. 610  
611 (10) Wintjes, N.; Bonifazi, D.; Cheng, F.; Kiebele, A.; Stöhr, M.; 612  
613 Jung, T.; Spillmann, H.; Diederich, F. *Angew. Chem., Int. Ed.* **2007**, *46*, 614  
615 4089–4092. 616  
617 (11) Seufert, K.; Auwärter, W.; Barth, J. V. *J. Am. Chem. Soc.* **2010**, 618  
619 *132*, 18141–18146. 620

- 593 (12) Tierney, H. L.; Murphy, C. J.; Jewell, A. D.; Baber, A. E.; Iski, E.  
594 V.; Khodaverdian, H. Y.; McGuire, A. F.; Klebanov, N.; Sykes, E. C. H.  
595 *Nat. Nanotechnol.* **2011**, *6*, 625–629.
- 596 (13) Auwärter, W.; Seufert, K.; Bischoff, F.; Ćeija, D.; Vijayaraghavan,  
597 S.; Joshi, S.; Klappenberger, F.; Samudrala, N.; Barth, J. V. *Nat.*  
598 *Nanotechnol.* **2012**, *7*, 41–46.
- 599 (14) Mannini, M.; Pineider, F.; Sainctavit, P.; Danieli, C.; Otero, E.;  
600 Sciancalepore, C.; Talarico, A. M.; Arrio, M.-A.; Cornia, A.; Gatteschi,  
601 D.; Sessoli, R. *Nat. Mater.* **2009**, *8*, 194–197.
- 602 (15) Gambardella, P.; Stepanow, S.; Dmitriev, A.; Honolka, J.; de  
603 Groot, F. M. F.; Lingenfelder, M.; Sen Gupta, S.; Sarma, D. D.;  
604 Bencok, P.; Stanesco, S.; et al. *Nat. Mater.* **2009**, *8*, 189–193.
- 605 (16) Bogani, L.; Wernsdorfer, W. *Nat. Mater.* **2008**, *7*, 179–186.
- 606 (17) Wende, H.; et al. *Nat. Mater.* **2007**, *6*, 516–520.
- 607 (18) Kong, J.; Franklin, N. R.; Zhou, C.; Chapline, M. G.; Peng, S.;  
608 Cho, K.; Dai, H. *Science* **2000**, *287*, 622–625.
- 609 (19) Varghese, O.; Kichambre, P.; Gong, D.; Ong, K.; Dickey, E.;  
610 Grimes, C. *Sens. Actuators, B* **2001**, *81*, 32–41.
- 611 (20) Seufert, K.; Bocquet, M.-L.; Auwärter, W.; Weber-Bargioni, A.;  
612 Reichert, J.; Lorente, N.; Barth, J. V. *Nat. Chem.* **2011**, *3*, 114–119.
- 613 (21) Schiffrin, A.; Riemann, A.; Auwärter, W.; Pennec, Y.; Weber-  
614 Bargioni, A.; Cvetko, D.; Cossaro, A.; Morgante, A.; Barth, J. V. *Proc.*  
615 *Natl. Acad. Sci. U. S. A.* **2007**, *104*, 5279–5284.
- 616 (22) Bonifazi, D.; Mohnani, S.; Llanes-Pallas, A. *Chem.—Eur. J.* **2009**,  
617 *15*, 7004–7025.
- 618 (23) Schlickum, U.; Decker, R.; Klappenberger, F.; Zoppellaro, G.;  
619 Klyatskaya, S.; Ruben, M.; Silanes, I.; Arnau, A.; Kern, K.; Brune, H.;  
620 Barth, J. V. *Nano Lett.* **2007**, *7*, 3813–3817.
- 621 (24) Wintjes, N.; Hornung, J.; Lobo-Checa, J.; Voigt, T.; Samuely,  
622 T.; Thilgen, C.; Stöhr, M.; Diederich, F.; Jung, T. *Chem.—Eur. J.* **2008**,  
623 *14*, 5794–5802.
- 624 (25) Theobald, J. A.; Oxtoby, N. S.; Phillips, M. A.; Champness, N.  
625 R.; Beton, P. H. *Nature* **2003**, *424*, 1029–1031.
- 626 (26) Stepanow, S.; Lingenfelder, M.; Dmitriev, A.; Spillmann, H.;  
627 Delvigne, E.; Lin, N.; Deng, X.; Cai, C.; Barth, J. V.; Kern, K. *Nat.*  
628 *Mater.* **2004**, *3*, 229–233.
- 629 (27) Stepanow, S.; Lin, N.; Barth, J. V.; Kern, K. *Chem. Commun.*  
630 **2006**, 2153–2155.
- 631 (28) Schull, G.; Douillard, L.; Fiorini-Debuischert, C.; Charra, F.;  
632 Mathevet, F.; Kreher, D.; Attias, A.-J. *Nano Lett.* **2006**, *6*, 1360–1363.
- 633 (29) Kühne, D.; Klappenberger, F.; Krenner, W.; Klyatskaya, S.;  
634 Ruben, M.; Barth, J. V. *Proc. Natl. Acad. Sci. U. S. A.* **2010**, *50*, 21332–  
635 21336.
- 636 (30) Spillmann, H.; Kiebele, A.; Stöhr, M.; Jung, T. A.; Bonifazi, D.;  
637 Cheng, F.; Diederich, F. *Adv. Mater.* **2006**, *18*, 275–279.
- 638 (31) Schiffrin, A.; Reichert, J.; Auwärter, W.; Jahnz, G.; Pennec, Y.;  
639 Weber-Bargioni, A.; Stepanyuk, V. S.; Niebergall, L.; Bruno, P.; Barth,  
640 J. V. *Phys. Rev. B* **2008**, *78*, 035424.
- 641 (32) Philp, D.; Stoddart, J. F. *Angew. Chem., Int. Ed.* **1996**, *35*, 1155–  
642 1196.
- 643 (33) Klug, A. *Phil. Trans. R. Soc. London B* **1999**, *354*, 531–535.
- 644 (34) Aggeli, A.; Nyrkova, I. A.; Bell, M.; Harding, R.; Carrick, L.;  
645 McLeish, T. C. B.; Semenov, A. N.; Boden, N. *Proc. Natl. Acad. Sci. U.*  
646 *S. A.* **2001**, *98*, 11857–11862.
- 647 (35) Kawasaki, T.; Tokuhira, M.; Kimizuka, N.; Kunitake, T. *J. Am.*  
648 *Chem. Soc.* **2001**, *123*, 6792–6800.
- 649 (36) Elemans, J. A. A. W.; Rowan, A. E.; Nolte, R. J. M. *J. Mater.*  
650 *Chem.* **2003**, *13*, 2661–2670.
- 651 (37) He, Y.; Ye, T.; Su, M.; Zhang, C.; Ribbe, A. E.; Jiang, W.; Mao,  
652 C. *Nature* **2008**, *452*, 198–201.
- 653 (38) Knowles, T. P. J.; Oppenheim, T. W.; Buell, A. K.; Chirgadze, D.  
654 Y.; Welland, M. E. *Nat. Nanotechnol.* **2010**, *5*, 204–207.
- 655 (39) Spillmann, H.; Dmitriev, A.; Lin, N.; Messina, P.; Barth, J. V.;  
656 Kern, K. *J. Am. Chem. Soc.* **2003**, *125*, 10725–10728.
- 657 (40) Ashkenasy, G.; Jagasia, R.; Yadav, M.; Ghadiri, M. R. *Proc. Natl.*  
658 *Acad. Sci. U. S. A.* **2004**, *101*, 10872–10877.
- 659 (41) Ruben, M.; Ziener, U.; Lehn, J.-M.; Ksenofontov, V.; Gütlich,  
660 P.; Vaughan, G. B. M. *Chem.—Eur. J.* **2005**, *11*, 94–100.
- (42) Blüm, M.-C.; Čavar, E.; Pivetta, M.; Patthey, F.; Schneider, W.-  
661 *D. Angew. Chem., Int. Ed.* **2005**, *44*, 5334–5337. 662
- (43) Clair, S.; Pons, S.; Brune, H.; Kern, K.; Barth, J. V. *Angew.*  
663 *Chem., Int. Ed.* **2005**, *44*, 7294–7297. 664
- (44) Staniec, P. A.; Perdigo, L. M. A.; Saywell, A.; Champness, N.  
665 R.; Beton, P. H. *ChemPhysChem* **2007**, *8*, 2177–2181. 666
- (45) Schlickum, U.; Decker, R.; Klappenberger, F.; Zoppellaro, G.;  
667 Klyatskaya, S.; Auwärter, W.; Neppel, S.; Kern, K.; Brune, H.; Ruben,  
668 M.; Barth, J. V. *J. Am. Chem. Soc.* **2008**, *130*, 11778–11782. 669
- (46) Ćeija, D.; Seufert, K.; Heim, D.; Auwärter, W.; Aurisicchio, C.;  
670 Fabbro, C.; Bonifazi, D.; Barth, J. V. *ACS Nano* **2010**, *4*, 4936–4942. 671
- (47) Liang, H.; Sun, W.; Jin, X.; Li, H.; Li, J.; Hu, X.; Teo, B. K.; Wu,  
672 K. *Angew. Chem., Int. Ed.* **2011**, *50*, 7562–7566. 673
- (48) Zhang, H. L.; Chen, W.; Huang, H.; Chen, L.; Wee, A. T. S. *J.*  
674 *Am. Chem. Soc.* **2008**, *130*, 2720–2721. 675
- (49) Cañas-Ventura, M. E.; Xiao, W.; Wasserfallen, D.; Müllen, K.;  
676 Brune, H.; Barth, J. V.; Fasel, R. *Angew. Chem., Int. Ed.* **2007**, *46*,  
677 1814–1818. 678
- (50) Kampschulte, L.; Werblowsky, T. L.; Kishore, R. S. K.;  
679 Schmittel, M.; Heckl, W. M.; Lackinger, M. *J. Am. Chem. Soc.* **2008**,  
680 *130*, 8502–8507. 681
- (51) de Oteyza, D. G.; Silanes, I.; Ruiz-Osés, M.; Barrena, E.; Doyle,  
682 B. P.; Arnau, A.; Dosch, H.; Wakayama, Y.; Ortega, J. E. *Adv. Funct.*  
683 *Mater.* **2009**, *19*, 259–264. 684
- (52) Shi, Z.; Lin, N. *J. Am. Chem. Soc.* **2010**, *132*, 10756–10761. 685
- (53) Jensen, S.; Greenwood, J.; Früchtl, H. A.; Baddeley, C. J. *J. Phys.*  
686 *Chem. C* **2011**, *115*, 8630–8636. 687
- (54) Shi, Z.; Lin, T.; Liu, J.; Liu, P. N.; Lin, N. *CrystEngComm* **2011**,  
688 *13*, 5532–5534. 689
- (55) Makoudi, Y.; Arras, E.; Kečija, N.; Krenner, W.; Klyatskaya, S.;  
690 Klappenberger, F.; Ruben, M.; Seitsonen, A. P.; Barth, J. V. *ACS Nano*  
691 **2012**, *6*, 549–556. 692
- (56) Clair, S. *Ph.D. thesis*, Ecole Polytechnique Federale de Lausanne,  
693 2004. 694
- (57) Clair, S.; Pons, S.; Seitsonen, A. P.; Brune, H.; Kern, K.; Barth, J.  
695 *V. J. Phys. Chem. B* **2004**, *108*, 14585–14590. 696
- (58) Kühne, D.; Klappenberger, F.; Decker, R.; Schlickum, U.; Brune,  
697 H.; Klyatskaya, S.; Ruben, M.; Barth, J. V. *J. Phys. Chem. C* **2009**, *113*,  
698 17851–17859. 699
- (59) Gonze, X.; Rignanese, G.-M.; Verstraete, M.; Beuken, J.-M.;  
700 Pouillon, Y.; Caracas, R.; Jollet, F.; Torrent, M.; Zerah, G.; Mikami,  
701 M.; et al. *Zeit. Kristallogr.* **2005**, *220*, 558–562. 702
- (60) Torrent, M.; Jollet, F.; Bottin, F.; Zerah, G.; Gonze, X. *Comput.*  
703 *Mater. Sci.* **2008**, *42*, 337. 704
- (61) Barth, J. V.; Weckesser, J.; Trimarchi, G.; Vladimirova, M.; De  
705 Vita, A.; Cai, C.; Brune, H.; Günter, P.; Kern, K. *J. Am. Chem. Soc.*  
706 **2002**, *124*, 7991–8000. 707
- (62) Klappenberger, F.; Cañas-Ventura, M. E.; Clair, S.; Pons, S.;  
708 Schlickum, U.; Qu, Z.-R.; Strunskus, T.; Comisso, A.; Wöll, C.; Brune,  
709 H.; Kern, K.; De Vita, A.; Ruben, M.; Barth, J. V. *ChemPhysChem*  
710 **2008**, *9*, 2522–2530. 711
- (63) Klappenberger, F.; Kühne, D.; Marschall, M.; Neppel, S.;  
712 Krenner, W.; Nefedov, A.; Strunskus, T.; Fink, K.; Wöll, C.;  
713 Klyatskaya, S.; Fuhr, O.; Ruben, M.; Barth, J. V. *Adv. Funct. Mater.*  
714 **2011**, *21*, 1631–1642. 715
- (64) Klappenberger, F.; Cañas-Ventura, M. E.; Clair, S.; Pons, S.;  
716 Schlickum, U.; Qu, Z.-R.; Brune, H.; Kern, K.; Strunskus, T.; Wöll, C.;  
717 Comisso, A.; De Vita, A.; Ruben, M.; Barth, J. V. *ChemPhysChem*  
718 **2007**, *8*, 1782–1786. 719
- (65) Klappenberger, F.; Kühne, D.; Krenner, W.; Silanes, I.; Arnau,  
720 A.; Garcia de Abajo, F. J.; Klyatskaya, S.; Ruben, M.; Barth, J. V. *Nano*  
721 *Lett.* **2009**, *9*, 3509–3514. 722
- (66) Klappenberger, F.; Kühne, D.; Krenner, W.; Silanes, I.; Arnau,  
723 A.; Garcia de Abajo, F. J.; Klyatskaya, S.; Ruben, M.; Barth, J. V. *Phys.*  
724 *Rev. Lett.* **2011**, *106*, 026802. 725
- (67) Krenner, W.; Klappenberger, F.; Kühne, D.; Diller, K.; Qu, Z.-  
726 R.; Ruben, M.; Barth, J. V. *J. Phys. Chem. Lett.* **2011**, *2*, 1639–1645. 727

- 728 (68) Decker, R.; Schlickum, U.; Klappenberger, F.; Zoppellaro, G.;  
729 Klyatskaya, S.; Ruben, M.; Barth, J. V.; Brune, H. *Appl. Phys. Lett.*  
730 **2008**, *93*, 243102–1–3.
- 731 (69) Kühne, D.; Klappenberger, F.; Decker, R.; Schlickum, U.; Brune,  
732 H.; Klyatskaya, S.; Ruben, M.; Barth, J. V. *J. Am. Chem. Soc.* **2009**, *131*,  
733 3881–3883.